Field experiment and image reconstruction using a Fourier telescopy imaging system over a 600-m-long horizontal path

Shu-hai Yu,[1,*] **Lei Dong,**[2] **Xin-yue Liu,**[2] **Xu-dong Lin,**[2] **Hao-ran Meng,**[2] **and Xing Zhong**[1,2]

[1]*Chang Guang Satellite Technology Co., Ltd, Crossing of North Yuanda Street and Longhu Road, Changchun 130033, China*
[2]*Changchun Institute of Optics, Fine Mechanics and Physics, Chinese Academy of Sciences, 3888 Dong Nanhu Road, Changchun 130033, China*
*Corresponding author: yushuhai_0707@sina.com

To confirm the effect of uplink atmospheric turbulence on Fourier telescopy (FT), we designed a system for far-field imaging, utilizing a T-type laser transmitting configuration with commercially available hardware, except for a green imaging laser. The horizontal light transmission distance for both uplink and downlink was ~300 m. For both the transmitting and received beams, the height upon the ground was below 1 m. The imaging laser's pointing accuracy was ~9.3 μrad. A novel image reconstruction approach was proposed, yielding significantly improved quality and Strehl ratio of reconstructed images. From the reconstruction result, we observed that the tip/tilt aberration is tolerated by the FT system even for Changchun's atmospheric coherence length parameter (r0) below 3 cm. The resolution of the reconstructed images was ~0.615 μrad. © 2016 Optical Society of America

1. INTRODUCTION

Fourier telescopy (FT) combines active laser imaging with integrative synthetic aperture technologies. The difference between the piston phases of a pair of broadcast beams is decoupled by using a phase closure method. As a candidate method for detecting small, dim, and distal targets, FT has been extensively studied over the past twenty years. Imaging of satellite orbits has developed along two different directions, depending on the satellite's orbit. One is the use of geosynchronous orbits (GEO) as imaging targets, such as in the GEO light imaging national testbed (GLINT) program. The other is the imaging for low orbits and fast-moving targets, such as the satellite active imaging national testbed (SAINT). However, the imaging fundamentals are the same for both of these applications. Since the beam diameter of a transmitting laser is always below 40 cm [1], as designed in the GLINT program, the impact of atmospheric turbulence of high modes on the imaging system is very subtle, and adaptive optics [2] is not required for reshaping the beams, which reduces the cost and complexity of the imaging system. The resolution can be improved by increasing the baseline length and the number of transmitters, similar to that for the very long baseline array technology. For GEO targets, the imaging resolution can reach 8 nrad [1]. This resolution is equivalent to that of a conventional ground telescope with an optical diameter of ~100 m. The

signal-to-noise ratio (SNR) of the reconstructed images can be easily increased by using the "light bucket" as a receiver.

Since the proposal of FT-based imaging, many researchers have simulated the fundamentals of this imaging system and designed and conducted experiments to confirm the system's feasibility and capability. Holmes developed the mathematical theory of imaging and laser transmitting arrays [3], which provided a foundation for the development of FT. Campbell experimentally obtained an angular resolution of 83 μrad [4]. Theoretical foundations of FT imaging and the effect of atmospheric turbulence on the FT system were extensively studied [5]. Furthermore, simulation studies were performed for GEO satellites and high-resolution reconstruction images were obtained. Laboratory and field work were performed for confirming the feasibility of FT imaging [6,7]. This work demonstrated the downlink horizontal transmission of 1.5 Km and confirmed that the FT imaging system is practically insensitive to the downlink atmospheric turbulence.

Compared with previous studies, the following are the novel achievements of the present work.

(1) We conducted a field experiment over a 600-m-long horizontal path, in which the heights of the transmitting beams were close to the ground. In other words, the horizontal distance from the transmitter to the target was ~300 m, and that from the target to the receiver was ~300 m. Compared with

previously reported results for near-field imaging, in which the distance from the imaging target to the laser transmitter was less than 5 cm, the overall light transmission distance was less than that in Ref. [7] restricted by the field experiment condition, but the beams' uplink distance was ~300 m for far-field imaging. We realized simultaneous uplink and downlink transmission, making the experimental system much more realistic.

(2) A T-type laser transmission configuration and a method for beam pointing were proposed using some mobile platforms. Along the x-axis, the maximal number of transmitting telescopes was 32, and the minimal spacing between adjacent telescopes was 4 cm. In other words, the scanning beam was moved in steps of 4 cm. The maximal diameters of the imaging system and the transmitting aperture were 128 cm and ~0.8 cm, respectively. A red laser was placed in the proximity of the target to guarantee the beams' pointing accuracy (e.g., the laser guide star technology [8]). Combining the positions of the spots' centroids collected using charge-coupled device (CCD) cameras yielded close-loop pointing of transmitting beams. A custom green laser was fixed on the transmitting platform for obtaining an interference fringe for the scanning target.

(3) The method of transmitting beams' scanning, a single Fourier component extraction and phase closure approaches were expounded and confirmed in computer simulations.

(4) A novel image reconstruction approach was proposed, the use of which improved both the imaging quality and Strehl ratio (SR) of an image. A small, dim imaging target (maximal and minimal scales of 3.2 mm and 0.37 mm, respectively) was reconstructed using main control software. The image resolution obtained using the proposed method was ~0.615 µrad.

This paper is divided into four sections. Section 2 describes the transmitter and receiver. Scan and demodulation methods of the T-type configuration are proposed in Section 3. Section 4 describes the software design and running results. In the last section, we present the image reconstruction approach and the results.

2. TRANSMITTER AND RECEIVER

A. Transmitting System

We have designed and built an experimental system based on the T-type laser transmitting configuration. As the T-type scan theory in Section 3 explains, to scan a target using three beams, one beam (the fixed beam) should be moved by one step in the x and y directions, while the other two beams (x and y scan beams) should be moved by a long distance in the x and y directions, respectively. Thus, the experimental system in the present study utilized mobile platforms with two short-displacement modes and two long-displacement modes.

Figure 1 shows the schematic of the transmitting system. Beam splitters (A1 and A2 are the 3/7 and 5/5 splitters, respectively), a reflection mirror (A3), and acousto-optic modulators (AOMs) were placed in the green laser box (denoted by the dotted line) and will be referred to as "the transmitting laser group" hereafter. The three AOM drivers are not phase-locked with respect to each other, but their frequency stability is better than 10E − 6. In other words, if the frequency is slightly shifted by 150 KHz, the resulting error will be ~0.15 Hz. This stability is sufficient for reconstructing images, which has been
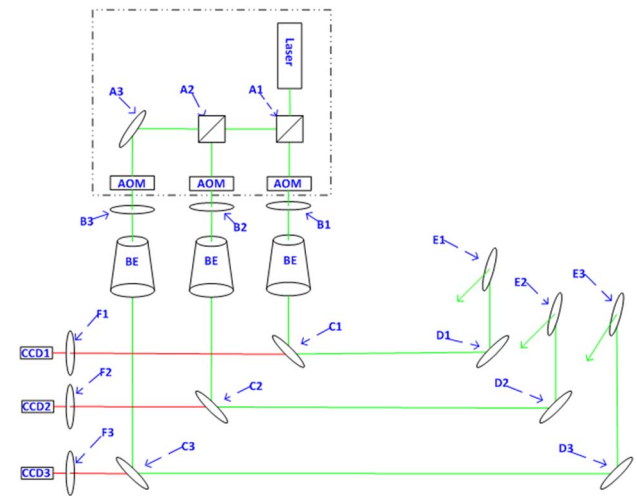

Fig. 1. Schematic of the transmitting system.

experimentally proven by us previously. A pair of beams with different polarizations reduces the contrast ratio of interference firings, constraining the SNR of the echo signal. This is likely to degrade the quality of image reconstruction. To avoid this, the polarizations of the three beams in our experimental system were maintained by using three half-wave plates (B1, B2, and B3). Then, the green lights were transmitted on the beam expanders to reduce the beams' diverging angle. The beams were reflected by dichroic beam splitters (C1, C2, and C3) that reflected the 532 nm (green) and transmitted the 635 nm (red) beams, and transmitted the beams into continuous mirrors (D1, D2, and D3). Finally, the green light beams were pointed to a target by pointing mirrors (E1, E2, and E3). The continuous mirrors of the fixed and x-axis scan beams were placed on mobile platforms to ensure that the beams could be reflected to the pointing mirrors when the platforms were moving. The continuous mirror of the y-axis scan beam was fixed on the optical platform. F1, F2, and F3 are filters that can block off the 532 nm stray light to avoid spot centroid calculation errors.

The specifications of the beam expander and the dichroic beam splitter are listed in Table 1.

Figure 2 shows the laser transmitting system. The CCD cameras collect spots of the red light for realizing automatic pointing. The pointing principle is described in the next section.

B. Automatic Pointing System

The target's spatial frequency components can be extracted using two interference beams. The components correspond to the intersection angle of the beams. A CCD camera was used for monitoring the position of three spots in the near-field

Table 1. Specifications and Components

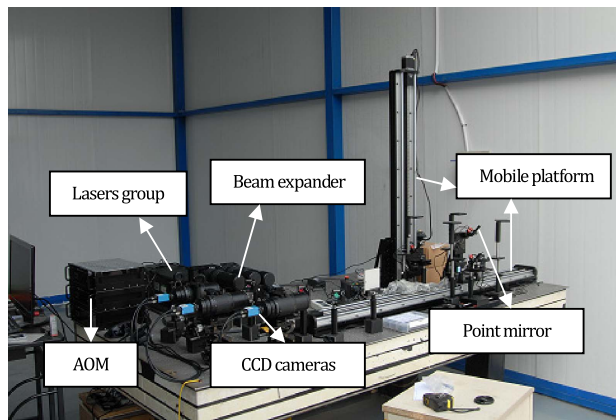| Name	Model	Manufacture
Beam expander	20DKIT-CI	Newport
Dichroic beam splitter	DCM13	Newport

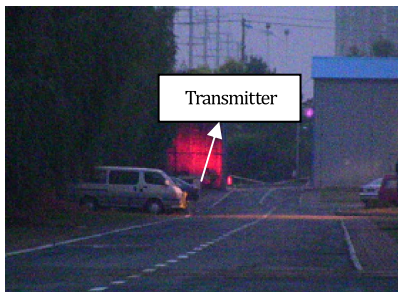**Fig. 2.**   Laser transmitting system.

Fig. 3.   Red laser light covers the transmitter.

experiment; however, this method is not suitable for far-field situations. Thus, we studied the beam pointing system.

The red laser was placed near the target, and the beam's diverging angle was increased using a beam expander, until the red light covered the entire transmitting configuration, as shown in Fig. 3.

Figure 4 illustrates the principle of automatic pointing. The green and red lights were spaced by dichroic beam splitter C1 in Figs. 1 and 4, which reflected the green and transmitted red beams. We also used three filters that blocked the green light and transmitted the red light, for preventing speckles of green light arriving at the CCD camera and affecting the spot centroid calculation. Thus, only red speckles could reach the CCD cameras after being transmitted through the pointing mirrors (E1, E2, and E3), the continuous mirrors (D1, D2, and D3)
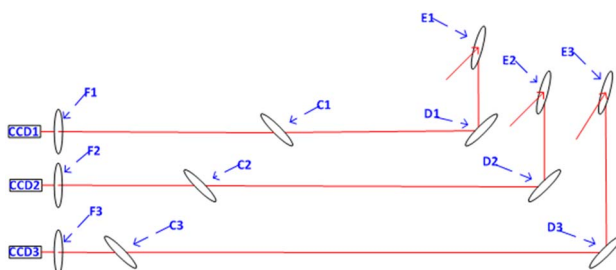

Fig. 4.   Schematic of the pointing system.

and the filters (F1, F2, and F3). The red and green lights were aligned along the same optical paths when they passed through the dichroic beam splitters (C1, C2, and C3) to the pointing mirrors (E1, E2, and E3); thus, automatic pointing could be realized by calculating the positions of spot centroids for images collected using the CCD cameras.

Spot centroid positions were at the centers of the CCD cameras during the initial operation. When one of the mobile platforms moves by the minimal separation distance (4 cm) and the pointing mirror is static, the central position of a spot collected by the corresponding CCD camera changes. The centroid can be returned to its initial position (the position error between the initial and post-movement positions is less than the setting threshold) by adjusting the pointing mirror. Collectively, Figs. 1 and 4 suggest that when the central position of a red speckle is at the center of the image of a CCD camera, the green light will accurately point to the target; in other words, the centroid of green beams will cover the target.

We used a rotating mechanical device (New Focus Company, series 8809) as the pointing motor and controlled it using a universal serial bus (USB). The pointing accuracy of the beam was determined by the pixel resolution of the CCD camera and the focal length of the lens that was placed before the camera. We used a Nikon commercial lens with a maximal focal length of 300 mm. The camera was a DMK 23G618 made by IMI, with a pixel resolution of 5.6 μm. The pointing to target was considered correct when the deviation of the position of the camera's spot centroid was below the setting threshold. In our experiment, the threshold was half a pixel and the pointing accuracy was ∼9.3 μrad. The middle of the beam deviated from the target by ∼2.79 mm at the target position.

C. Parameters of Green Laser and Mobile Platforms

Laser performance is the one of several important subsystems for the performance of the FT system. The laser should have good spatial interference and be a single mode. For our field experiments, we designed the green laser manufactured by the Changchun New Industries Optoelectronics Technology Co., Ltd. The main technical characteristics of this laser are listed in Table 2.

There are three common configurations of the transmitting system: T-type, circle-type [9], and Y-type. In Refs. [6,10] and [11], T-type scans were realized by rotating prisms using a stepping motor for near-field experiments. We used translation stages with a large travel distance for conducting the uplink far-field experiment. The technical characteristics of the four mobile platforms are listed in Table 3.

D. Receiver

Contrasted with the transmitter, the receiving system is very simple. The GLINT project will use heliostats without

Table 2.   Parameters of the Green Laser

Wavelength	Interference Length	Power	Polarization Ratio	Mode
532 nm	>10 m	>2.5 W	>50:1	Single

Table 3. Parameters of the Mobile Platforms

Number of Platform	1	2	3	4
Max journey (cm)	10	4	150	100
Resolution (mm)	0.01	0.00025	0.0125	0.0125

Table 4. Parameters of the Receiving Mirror

Diameter	Radius of Curvature	Reflectance
600 mm	3 m	>80%

considering their phase aberrations. In our system, the receiver was the secondary mirror, as described previously [12]; its main parameters are listed in Table 4. Because we used a specular reflection object, the energy was nearly completely echoed. According to the conclusion in Ref. [13], the SNR of the received signal is so high that there is no need to consider the effect of the speckle noise. However, in real imaging projects (such as GLINT and SAINT programs), this issue should be accounted for. Diffuse reflection, longer transmitting distances, and larger receivers will be addressed in the near future. The level of the residual speckle noise will also be discussed.

The light speckle was received and condensed by the condenser lens, and then collected using the photomultiplier tube (PMT). Figure 5 shows the receiver equipment, utilizing the PMT model P30A-05.

3. SCAN AND DEMODULATION METHODS OF T-TYPE CONFIGURATION

The T-type scan strategy can be divided into four steps, as shown in Figs. 6(a)–6(d). Taking as an example a 33 × 17 array of extracted spatial frequencies, the specific scan methods are as follows.

(1) The x-axial scan

Figure 6(a) shows the trajectory of the x-axial scanning beam. The closed green square and the closed green triangle represent a stationary beam and a shear one [3,14], respectively, and are stationary. The closed green circle is a scanning beam. The scanning beam is at (2, 0) in step 1, and collects the returning time-encoded signal after the pointing mirrors have closed point-to-target. Then, the scanning beam moves one

Fig. 5. Receiver equipment.

step (4 cm) to (3, 0) by controlling its mobile platforms, as is shown for step 2, and the process repeats to collect another signal. The above scanning operations are repeated until the scanning beam reaches (16, 0), as is shown for step 15.

(2) The y-axial scan

The circle represents a y-scan beam in Fig. 6(b). The square and triangle are as defined above, and are stationary. The scanning beam is placed at (0, 2) in step 1. The process of signal collection, similar to that for the x-axis scanning, is repeated until the beam arrives at (0, 16).

Please note that the beat frequencies of shear to fixed beam, scanning to shear beam, and scanning to fixed beam, were 50 KHz, 100 KHz, and 150 KHz, respectively, for the x- and y-axial scanning.

(3) The first quadrant scan

The square represents the stationary beam and remains static during the first and second quadrant scans. The circle and the triangle represent the x-scan and y-scan beams, respectively.

The x- and y-scan beams are placed at (1, 0) and (0, 1), respectively, as is shown in Fig. 6(c) for the start stage. The x-scan beam moves to (16, 0) step by step, along with the x-axis in the forward direction as is shown in the x-axis forward scanning (XFS) stage. This procedure is the same as that for the x-axial scan processing in Section 1. Then, the y-scan beam moves to (0, 2) as is shown in the y-axis moves minimal separation (YMMS) stage. The x-scan beam returns to (0, 1) in the backward direction (XBS) step by step, and then the y-scan beam moves to (0, 3) from (0, 2). The XFS and YMMS steps are repeated until the x- and y-axis scanning beams reach (1, 0) and (0, 16), respectively.

(4) The second quadrant scan

The x-scan and y-scan beams are placed at (–1, 0) and (0, 1), respectively, as is shown in Fig. 6(d). The second quadrant scan is similar to that for the first quadrant, except that now the x-axis scan beam moves along the negative x-axis. First, the x-scan beam moves to (–16, 0) step by step, as is shown in the XBS stage. Then, the y-axis scan beam moves to (0, 2) as is shown in the YMMS stage. These steps are repeated until the x- and y-scan beams reach (–1, 0) and (0, 16), similar to what was described for the first quadrant scan.

The beat frequencies of fixed to x-scan beam, y-scan to x-scan beam, and y-scan to fixed beam, were 50 KHz, 150 KHz, and 100 KHz, respectively.

The methods for phase closure and extraction of a single Fourier component of a target are the same as those for spot-plane scans in x- and y-axial scans. The equations and analysis are explained in detail elsewhere [5]. Taking the x-axis scan as an example, using the phase closure method and ignoring constants yields a ratio, denoted $R(k_m)$:

$$R(k_m) = \frac{M_{m,0}}{M_{m,1}M_{1,0}} = \frac{O(m\Delta k_x)}{O((m-1)\Delta k_x)O(\Delta k_x)}. \quad (1)$$

Here, the subscripts 0, 1, and m represent the fixed, shear, and scan beams, respectively, and describe the coordinates of the three beams on the x axis, for forming a specific fringe pattern. The index m satisfies $2 \leq m \leq 16$. M is the measured Fourier component's yield by transmitting a fringe Fourier
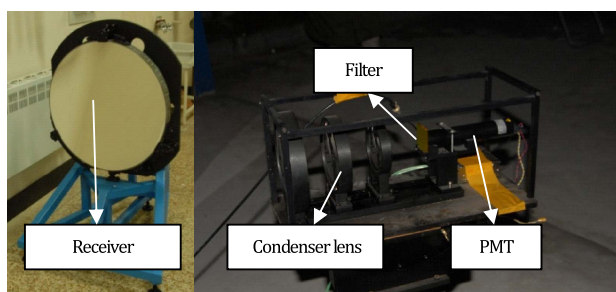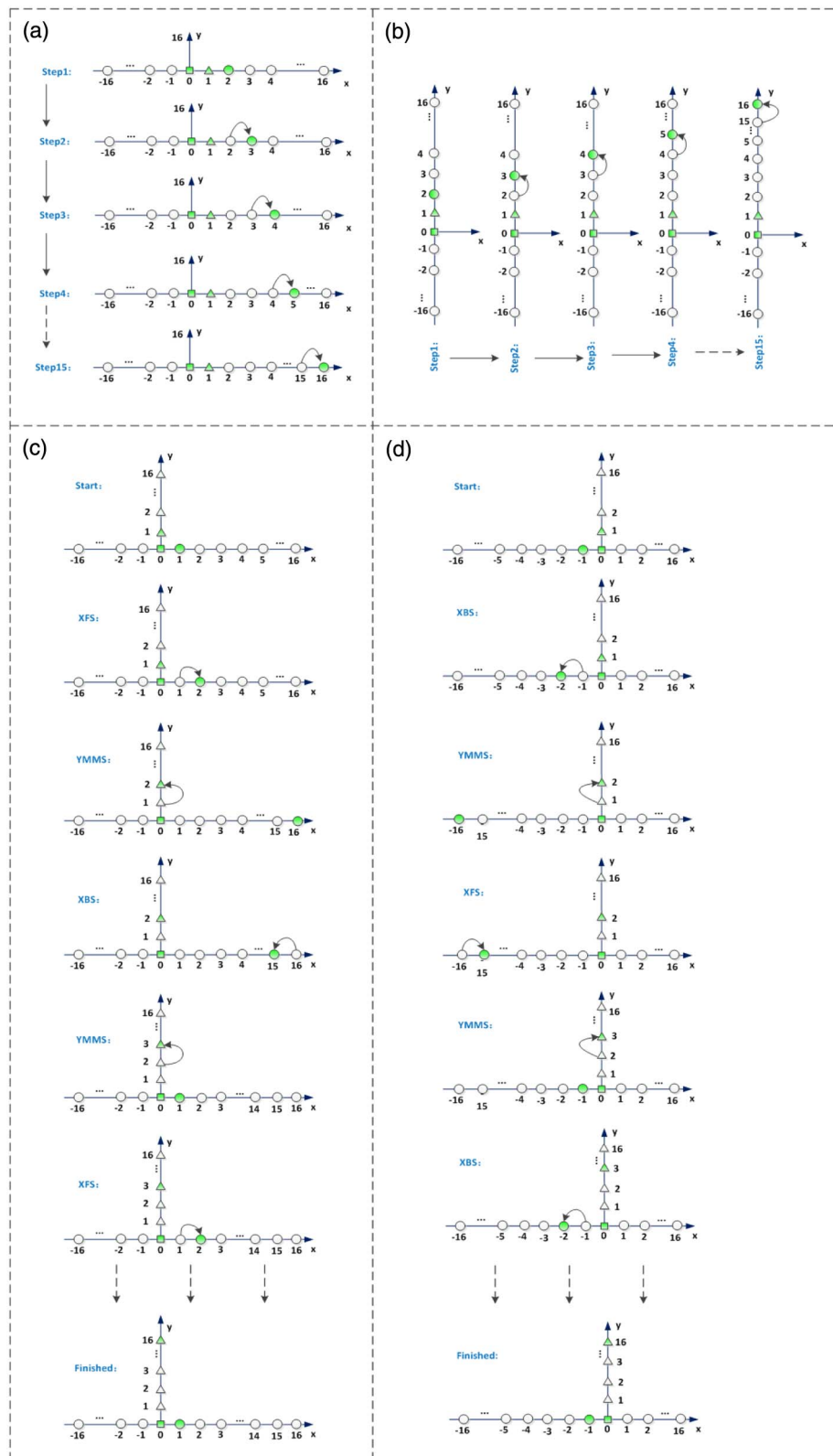
Fig. 6.   Schematic of T-type transmitter scanning.

demodulation. The fringe is formed by two beams corresponding to the subscripts. Δk_x is the minimal spatial frequency of a target extracted by the two beams in the x direction. $O(m\Delta k_x)$

is the single Fourier component of the target extracted by the finger of scanning and fixed beams, when the scanning beam is at $(m, 0)$.

Using uniform separation of transmitting telescopes configuration in our experiment, the single frequency component [5] of a target can be obtained in terms of multiple consecutive ratios from the ratio $R(k_m)$, as follows:

B. Analysis of Main Control Function

The software needs to satisfy several functions, such as the mobile platform and pointing mirror controls, PMT signal collection, and calculating centroids of spots images collected by the

$$
\begin{cases}
O(\Delta k_x) = R(k_1) = 1 \\
O(2\Delta k_x) = R(k_2)R(k_1) = O(2\Delta k_x)/O(\Delta k_x)/O(\Delta k_x) \\
\quad = O(2\Delta k_x)/O^2(\Delta k_x) \\
O(3\Delta k_x) = R(k_3)R(k_2)R(k_1) = O(3\Delta k_x)/O(2\Delta k_x)/O(\Delta k_x) \\
\quad \times O(2\Delta k_x)/O^2(\Delta k_x) \\
\quad = O(3\Delta k_x)/O^3(\Delta k_x) \\
\dots \\
O(m\Delta k_x) = R(k_m)R(k_{m-1})\cdots R(k_2)R(k_1) = O(m\Delta k_x)/O^m(\Delta k_x)
\end{cases}
. \tag{2}
$$

There are only remaining frequency components of the target except $O(\Delta k_x)$ in the above equation. The magnitude of $O(\Delta k_x)$ is not important for the reconstruction process, and its phase merely shifts the overall reconstructed image.

It should be noted that there are some differences between the phase closure technologies of T-type and spot-plane scan methods. The quadrant phase closure is

$$
R_q(k_{-m,n}) = \frac{M_{-m,n}}{M_{0,-m}M_{n,0}} = \frac{O(-m\Delta k_x + n\Delta k_y)}{O(-m\Delta k_x)O(n\Delta k_y)}, \tag{3}
$$

where m and n are the x-scan and y-scan beam coordinates, respectively, $-16 \leq m \leq 16$, $m \neq 0$, $1 \leq n \leq 16$ in our experiment, $O(-m\Delta k_x) = O(m\Delta k_x)^*$, with the asterisk denoting the conjugate algorithm. The single spatial frequency of the axial component is obtained from the axial scan, using Eq. (2). Thus, the quadrant component can be calculated from Eq. (4), and it does not require iterative calculation:

$$
O(m\Delta k_x + n\Delta k_y) = R_q(k_{m,n})O(m\Delta k_x)O(n\Delta k_y). \tag{4}
$$

The detailed description of the phase closure and single component extraction methods for the quadrant scan is provided in Ref. [15].

4. SOFTWARE DESIGN

A. Algorithm Simulation

In this section, the algorithm's validity was confirmed in computer simulations. We used a simple two-bar image as an imaging target for conveniently measuring the two-bar gap and the horizontal scale for easy validation of the imaging system's resolution. Figure 7 shows the simulation content and Fig. 8 shows the results obtained without considering the effect of atmospheric turbulence. From Eqs. (2) and (4), owing to the piston aberration (phase of $O(\Delta k_x)$ and $O(\Delta k_y)$), the reconstruction image is shifted in the x- and y-axis directions, as is shown in Fig. 8(b). A triple spatial extension method was adopted for displaying four integrated imaging targets, as is shown in Fig. 8(c). In other words, the middle image was filled in the right figure along with row and column. The algorithm was validated using the reconstructed images.

CCD cameras and image reconstruction. This requires simultaneously controlling the four mobile platforms (the first one is used for the x-axis scan, the second one is used for the y-axis scan, and the remaining platforms are the short-displacement one for the fixed beam scans in the x and y directions, respectively), three pointing mirrors, three CCD cameras, and one PMT.

During the field experiment, the mobile platform sometimes ignored the motion command, which introduced an error into the system scan. The long-distance travel stage was operated in an open loop; thus, no feedback was received when the stage was not successful in moving to the correct position. By estimating the different positions of spot centroids from CCD cameras, we determined whether the platform had moved to the setting position. This method was used in the experimental
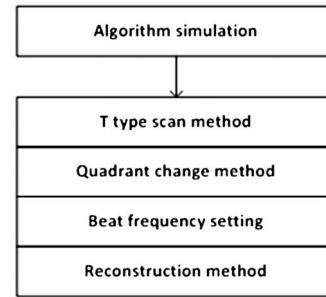
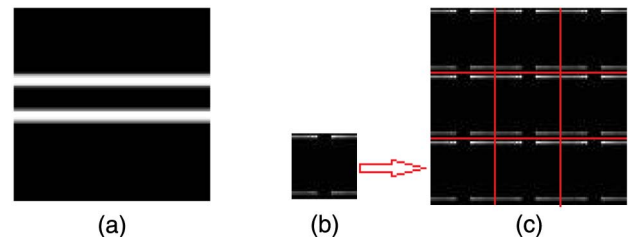

Fig. 7. Content of simulation.

Fig. 8. Results of the simulation. (a) Simulation target; (b) reconstruction image; (c) spatial extension.

system for uplink and downlink of light that were each transmitting 46 m in the laboratory. When the difference was less than the setting threshold, we considered that the platform did not move, and then stopped the pointing and signal collection, and continued to send motion commands until the platform had moved correctly. We obtained satisfactory results and reconstructed high-quality images of the target using this method.

In contrast with the laboratory experiment, in reality the centroid of a spot image sometimes changed very fast and significantly, even more than the setting threshold when the mobile platform was static, owing to atmospheric turbulence. At the same time, the centroid often varied less than the setting threshold when the platform moved correctly. Thus, the setting threshold method did not satisfy the field experiment requirements. Sometimes, people and/or cars appeared near the experiment area, which introduced light interference and caused experimental failure. Therefore, we designed the scan function to start at an arbitrary transmitter position and continue scanning when there was a platform or light-interference error.

C. Software Design

The interface for the main control software was programmed in Visual C++ (VC++). Figure 9 shows the software flowchart and Fig. 10 lists its main functions.

The enforcement steps are described in the following:

• Initialize four mobile platforms, three pointing units, one PMT, three CCD cameras, and monitored their status.
• Control a mobile platform to move one step in the setting direction. Then, collect a spot image using a CCD camera and calculate its centroid.
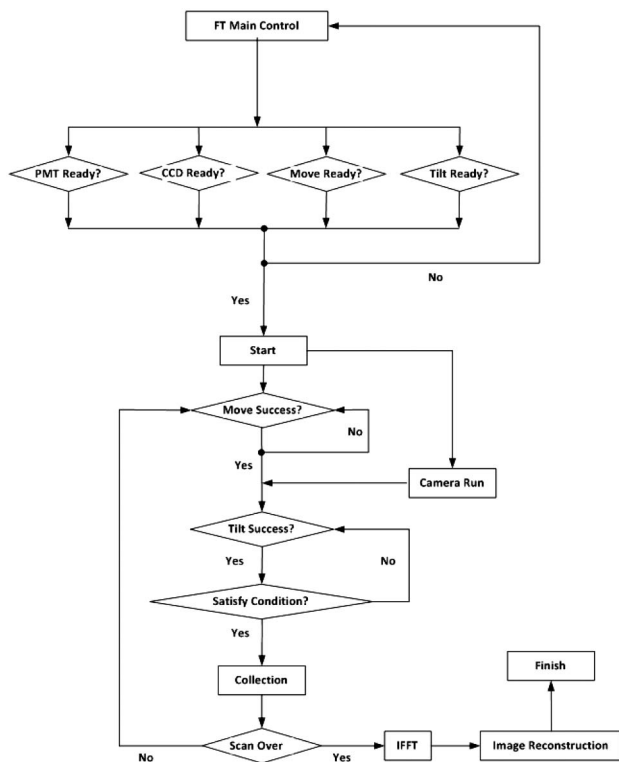
Fig. 9.   Software flowchart.
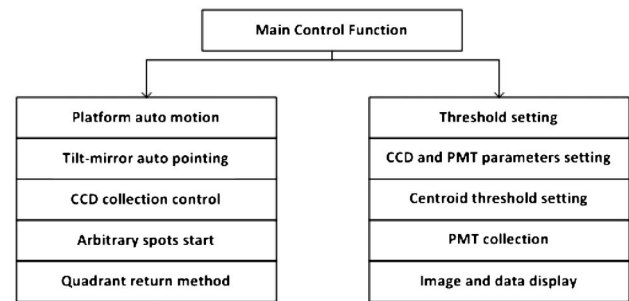
Fig. 10.   Main functions of the software.

• If any platform ignores the motion command or if a system error appears, operate the continuous scan method (arbitrary start spots).
• After moving the platform, control pointing mirrors to the pointing target until the centroids of images of the three CCD cameras are all less than the setting threshold.
• Control the PMT to collect the time-encoded signal reflected by the target.
• To ensure that the CCD camera can collect the red light speckle, we propose a half-axial return method, in which the y-axial scan is performed after the x-axial scan, the first quadrant scan is performed after the y-axial scan, and the second quadrant scan is performed after the first quadrant scan.
• Repeat the second step as shown in Fig. 6, until finishing the second quadrant scan and extracting all of the spatial frequency components.
• Use the phase closure method on the time-encoded signal and calculate the single frequency component from Eqs. (1)–(4).
• Use the inverse fast Fourier transform (IFFT) method for the matrix of single frequency components to reconstruct the target's image.

The reconstruction image algorithm was implemented in MATLAB, and the monitoring of the PMT collection time-encoded signal was performed in LabView.

5. RESULTS AND ANALYSIS

A. Main Control Software and Beam Control Result

The interface of the main control procedure is shown in Fig. 11. Area A is the monitor interface, which monitors the motion of the mobile platforms, the status of the pointing mirrors, and the collection of time-encoded signals by the PMT; area B is the folder with the file that holds the collected signal; area C shows the spot images of the three CCD cameras; and area D shows the interface, such as that for setting the parameters of the PMT, the positions of the centroids of the three images collected by the CCD cameras, the continuous scan, and system control buttons. The software can realize the beams' automatic scanning target and PMT collection signals.

Figures 12(a) and 12(b) show the images of the T-type transmitting laser and the pointing to the target, respectively. The relation between the transmitter and receiver is plotted in Fig. 13.
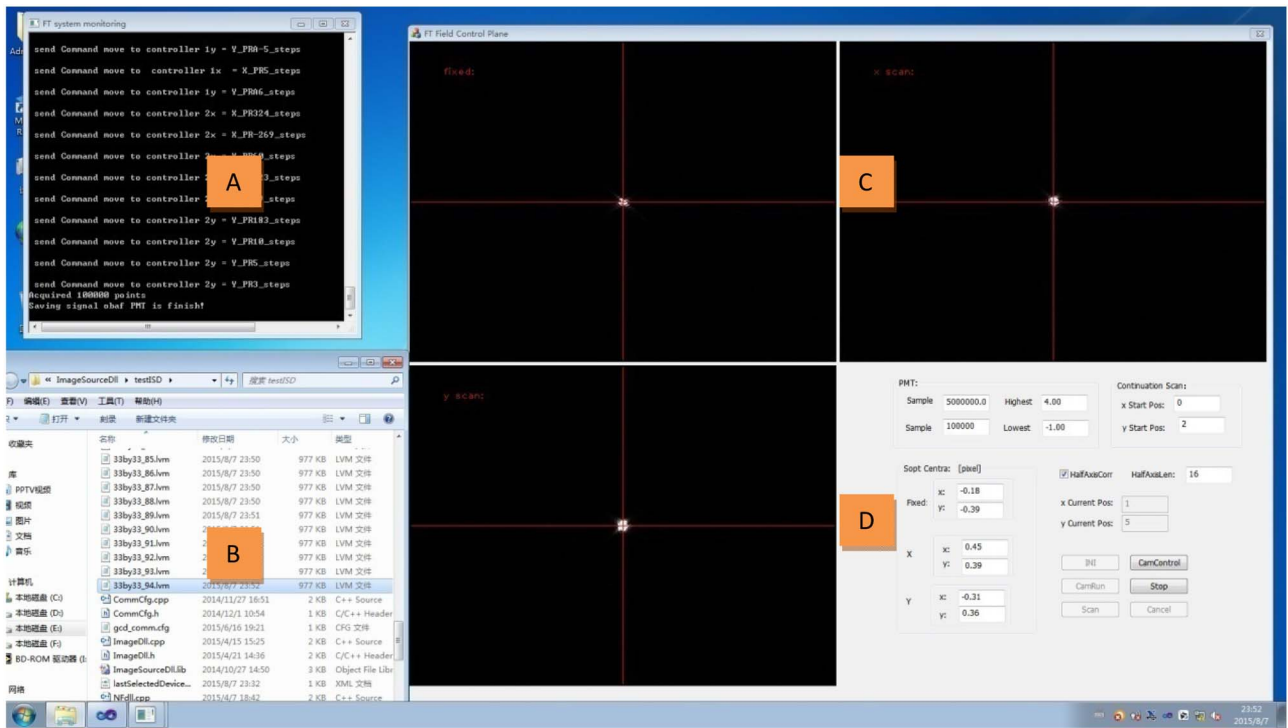
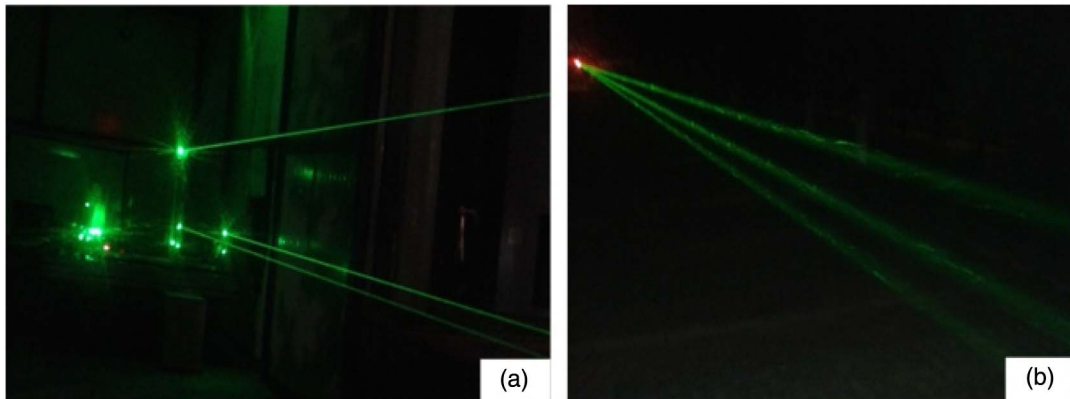**Fig. 11.** Interface of the main control software.

Fig. 12. (a) Transmitting laser; (b) pointing to the target.

B. Image Processing

The main experimental parameters are listed in Table 5.

The experimental protocol was as follows:

• Adjust the beams' power and polarization, as listed in Table 6.

• Ensure that the beams are accurately pointing to the target by manually adjusting the mobile platforms and pointing mirrors.

• Manually adjust the direction and pitching of the CCD cameras to ensure the centroids are at the centers of the cameras (initial calibration), as shown in Fig. 14.

• Move the three beams of the transmitting system to the origin (0, 0) by controlling the motion platforms.

• Start automatic scanning by running the main control procedure as shown in Fig. 11.

• Reconstruct the target image using the reconstruction procedure.

The time-encoded signal collected by the PMT and its Fourier demodulation are shown in Fig. 15. Three peaks can be seen in the right image at the frequencies of 50 KHz, 100 KHz, and 150 KHz, corresponding to the setting beat frequencies.

Minimal spatial frequency was calculated as described in Ref. [5]:

$$K_{1,0} = k_0 d/z, \tag{5}$$
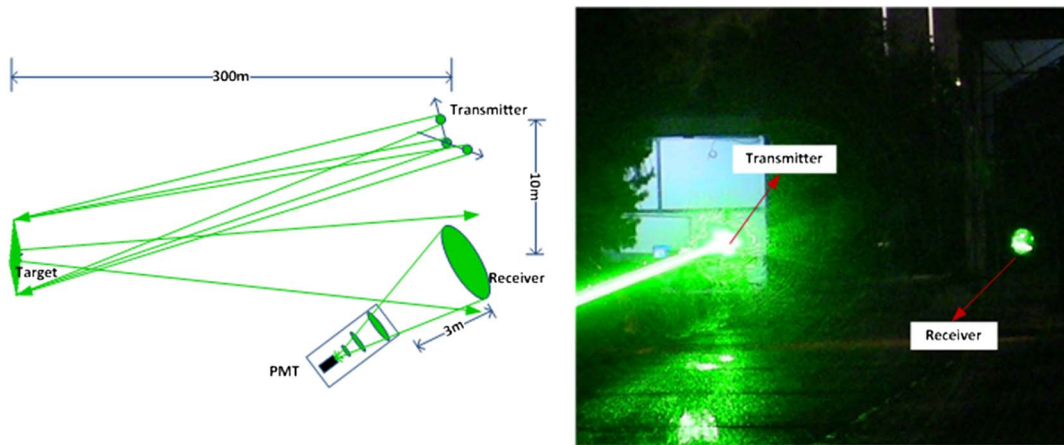
Fig. 13.   Relation between the transmitter and the receiver. The left panel shows the concept figure, and the right panel shows the actual implementation.

Table 5.   Parameters of the Experimental System

Minimal Separation	Pointing Threshold	Beat Frequency	Collection Frequency	Number of Transmitters
4 cm	0.5 pixel	50, 100, 150 KHz	5 MHz	33×17

Table 6.   Power and Polarization of Transmitting Beams

Beam Number	Power (mW)	Polarization
0	193	vertical
1	260	vertical
m	170	vertical

where k_0 is the light-wave wavenumber and $k_0 = 2\pi/\lambda$, λ is the laser wavelength, Z is the imaging distance, and d is the minimal separation. The frequency is the reciprocal of the target's linear size:

$$K_{1,0} = 2\pi/L. \qquad (6)$$

L is the target's linear size.
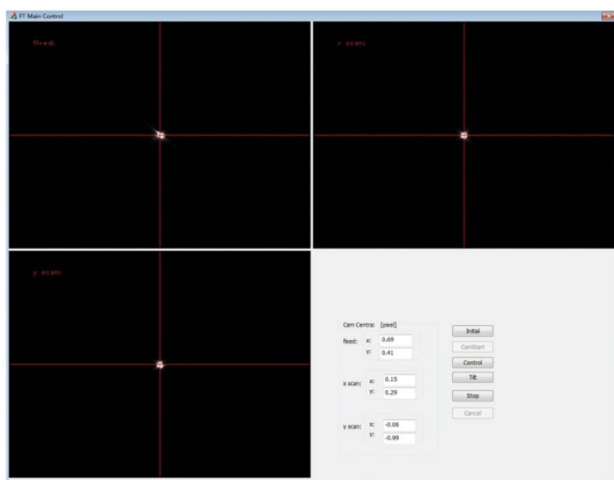
Fig. 14.   Initial calibration.
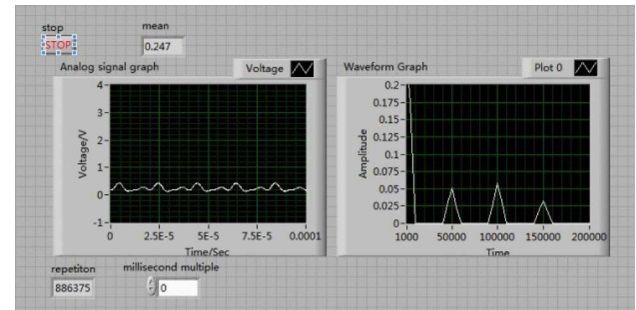
Fig. 15.   Interface of the PMT signal collection system.

Given this, the field-of-view (FOV) was determined by the minimal separation of two beams in the FT system:

$$\text{FOV} = L = \lambda Z/d. \qquad (7)$$

In our field experiment, we set $\lambda = 532$ nm, $Z \approx 300$ m, and $d = 4$ cm; thus, FOV ≈ 3.99 mm.
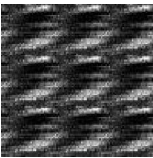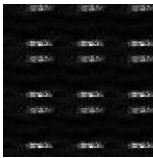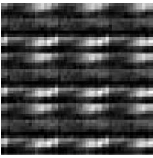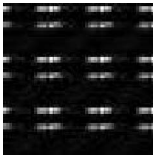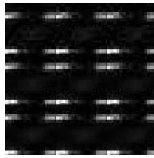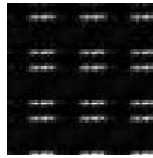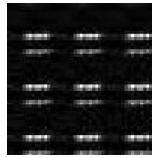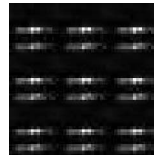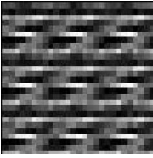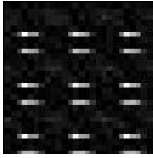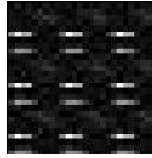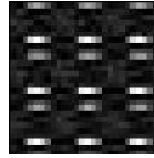
C. Analysis of Atmospheric Turbulence and Image Reconstruction Approach

In our experiment, the sampling frequency of the PMT was 5 MHz, and 100 points were collected in each cycle to satisfy the following Eq. (8). Each triple was sampled 1000 periods:
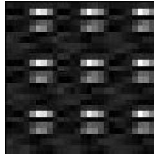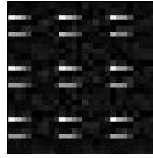
$$N\Delta\omega T = 2n\pi. \qquad (8)$$

In Eq. (8), N is the sampling number, T is the sampling time, $\Delta\omega$ is the beat frequency as listed in Table 5, and n is an integer. A useful reconstruction method involves demodulating each period and averaging over 1000 demodulations, or demodulating 10 periods and averaging over 100 times [14]:

Table 7. Original Reconstructed Images for the Three Experiments

Num	AOD	DSP:12th	DSP:334th	DSP:535th	DSP:848th	DSP:928th
1						
2						
3						

$$M_{m,n} = \frac{1}{N_p} \sum_{p=1}^{N_p} O_p(m\Delta k_x + n\Delta k_y) \exp(i\Delta\omega_{m,n} + i\Delta\varphi_{m,n,p}).$$

$$(9)$$

In Eq. (9), N_p is the number of sampling periods and O_p is the demodulation frequency of the target of a p-th cycle. We adopt the phase closure method for approximating the reconstruction image; this method is summarized in Eqs. (1)–(4). This reconstruction method was adopted in some previous studies [7,12,15,16] and is herein called averaging over demodulations (AOD). It is obvious that reconstructed images are seriously distorted by the AOD method, which fails to resolve even the imaging targets, as shown in Table 7. The overall sampling time was 20 ms for 1000 cycles, which is 20 µs for one cycle, while the frequency of atmospheric turbulence events is higher than 1 KHz [17]; thus, piston aberration must be different for different sampling periods. We propose that owing to this difference, the reconstruction images experience random shifts in the spatial domain during demodulation periods, which contributes to distorting the reconstruction image.

If the difference is subtle and the mean is close to zero, the AOD method is likely to be useful for reconstructing the target. The phase for 1000 cycles of demodulation is shown in Fig. 16 for the first imaging experiment. Clearly, the phase variance is too high for reliable image reconstruction using the AOD approach.

To check the validity of the above analysis, we attempted to demodulate a single period (DSP) for recovering the target. Table 7 shows the results of three experiments in which we used the same target with different resolutions. The number of spatial frequencies was 542, 142, and 38, in the first, second, and third experiment, respectively. Figure 6 shows that the motion of the x-axis and y-axis scan beams is limited to (16, 0) and (0, 16) in the first experiment, corresponding to 542 spatial frequencies, while the scenario with 142 frequencies (second experiment) corresponds to the (8, 0) and (0, 8) coordinates. The second and third recovered images are interpolated to 99 pixels × 99 pixels for convenient contrast with the first. The same number of single periods was adopted for all triple multiples. We selected five representative results among 1000 periods; these are shown in the third to seventh columns (for the DSP method). Some of the reconstructed images were slightly distorted, but overall their quality was better than those reconstructed using the AOD method. The conclusion that the images reconstructed using the DSP methods are randomly shifted in the spatial domain during different demodulation periods is also confirmed by inspecting the images in Table 7. This phenomenon is similar to the luck imaging technology [18,19]. Comparing the two approaches, we propose to use the DSP approach for avoiding reconstruction distortion.
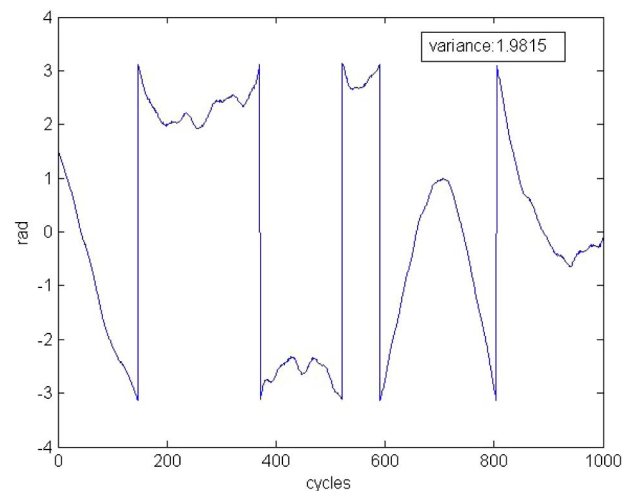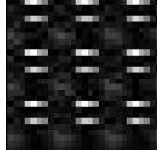

Fig. 16. Phase demodulation in the first experiment.

Table 8.   Images Obtained Using the APTD Approach

1	2	3

Although demodulation of one period can yield a good image, there are a total of 542,000 cycles in the scan configuration in Fig. 6, and it would be quite time-consuming to demodulate each period for determining the best one. In our experiment, single period demodulation was useful, owing to the high SNR of the encoded signal, but in an actual imaging system, the SNR is likely to be quite low, so it becomes necessary to sample multiple periods. The AOD approach was invalidated in Table 7; thus, we first demodulated each sampling period and then adopted the phase closure method for dropping out the piston aberration. Taking the x-axis scan as an example, the demodulation is

$$SM_{nu} = M_{m,0} = O(m\Delta k_x)\exp(i\Delta\omega_{m,0} + i\Delta\varphi_{m,0}). \quad (10)$$

The individual columns of the matrix SM_{nu} describe the demodulation of nu-th beat frequency for each cycle. Adopting the phase closure for each of the three demodulations allowed us to easily eliminate the piston aberration during a single sampling period, and obtain a triple, denoted a column vector ST (1000 elements):

$$ST = SM_3/SM_2/SM_1 = M_{m,0}/M_{m-1,0}/M_{1,0}. \quad (11)$$

Adopting the iteration calculation, similar to Eq. (2), allowed us to obtain single-frequency components of the target, given in Eq. (12). The phase of the mean of $M_{1,0}$ is denoted $\bar{\varphi}_{1,0}$, so $O(m\Delta k_x)$ introduces a random phase $m \times \bar{\varphi}_{1,0}$ that merely shifts the overall reconstructed image. The reconstructed images, shown in Table 8, have better quality. This reconstruction approach is herein called averaging phase triple demodulations (APTD):

$$\begin{cases} O(\Delta k_x) = \frac{1}{N_p}\sum_{p=1}^{N_p} M_{1,0} \\ O(2\Delta k_x) \approx \frac{1}{N_p}\sum_{p=1}^{N_p}[ST(p)O(\Delta k_x)O(\Delta k_x)] \\ O(3\Delta k_x) \approx \frac{1}{N_p}\sum_{p=1}^{N_p}[ST(p)O(2\Delta k_x)O(\Delta k_x)] \\ \dots \\ O(m\Delta k_x) \approx \frac{1}{N_p}\sum_{p=1}^{N_p}[ST(p)O((m-1)\Delta k_x)\dots O(\Delta k_x)] \end{cases} \quad (12)$$

Tip/tilt aberration is another factor affecting the performance of the FT imaging system, and this effect was explored in Ref. [20] for the GLINT program. There is little difference between our experimental system and the GLINT system, which is the angle between two arbitrary beams. This angle was ~4 cm/300 m ≈ 0.13 mrad in our experimental system, which is larger than the isoplanatic angle on the order of μrad. However, the error introduced by the tip/tilt turbulence can be tolerated by the reconstruction results. Put differently, if a

Table 9.   Image SRs

	APTD	AOD	12th	334th	535th	848th	928th
1	0.6650	-	0.6141	0.6022	0.6055	0.6395	0.6025
2	0.7227	-	0.7704	0.7586	0.6116	0.7429	0.7203
3	0.6931	-	0.6260	0.5796	0.6715	0.6394	0.6854

correct method is chosen for dealing with the piston aberration, high-resolution images can be obtained.

D. Image and Resolution Analysis

The image SR was computed by comparing the intensity distribution for the reconstructed image with that of the original image [5,14]. A cross-correlation between the two distributions was calculated as follows:

$$H(x,y) = O_T \otimes O_R$$
$$= \iint I_T^*(k_x, k_y)I_R(k_x, k_y)\exp(-i2\pi(k_x f_x + k_y f_y))\mathrm{d}x\mathrm{d}y, \quad (13)$$

where O_T and O_R are the truth and reconstructed image amplitude distributions. I_T and I_R are the Fourier transforms of the truth and reconstructed image amplitude distributions. Then, the SR is

$$\text{SR} = \frac{\max|H(x,y)|^2}{\iint O_T^*(x,y)O_T(x,y)\mathrm{d}x\mathrm{d}y \iint O_R^*(x,y)O_R(x,y)\mathrm{d}x\mathrm{d}y}. \quad (14)$$

The SRs of images are listed in Table 9. The quality of images reconstructed using the AOD approach was too low to resolve the target, precluding the calculation of SR.

To test the imaging system's resolution, we conducted another imaging experiment, for a smaller target; the targets are shown in Fig. 17. We also used the global phase closer (GPC)
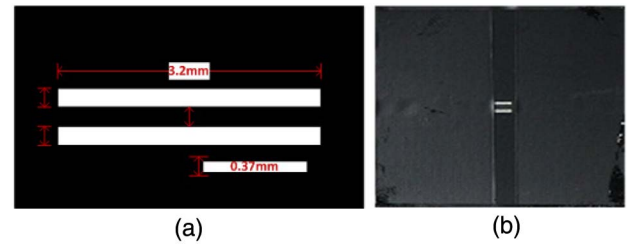

Fig. 17.   Reconstructed images. (a) Designated target; (b) real image of target.
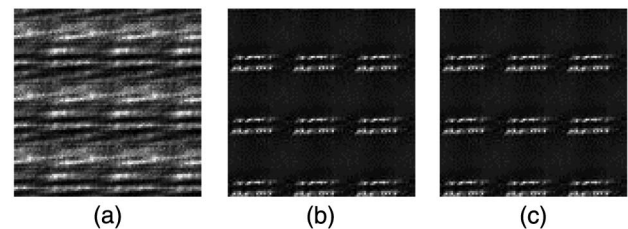

Fig. 18.   Reconstructed images for a smaller target. (a) AOD approach; (b) APTD approach; (c) GPC approach.

reconstruction method to recover the image. The SRs of using the APTD and GPC methods are 0.6790 and 0.6785, respectively. The results of APTD and GPC are very similar, because we simultaneously transmit three beams; the amount of beams is smaller than the SAINT program, although the GPC can improve the quality of image in the SAINT.

The reconstructed images obtained using the three approaches are shown in Fig. 18.

The imaging resolution, IR, was calculated as follows:

$$IR = D_{space}/Z = 0.37 \text{ mm}/300 \text{ m} \approx 1.23 \text{ μrad}. \quad (15)$$

There are two pixels between the two bars of the reconstructed images in Fig. 18, so the resolution can be estimated as $1.23/2 = 0.615$ μrad. Yet it is difficult to print the appropriate target to check the resolution limit.

6. CONCLUSIONS

The goal of this experiment was to investigate the effect of uplink atmospheric turbulence [21] on the FT imaging system. Adoption of a long-distance mobile platform replaced a rotation prism for realizing a T-type transmitting configuration for far-field imaging. The feasibility and validity of the beams' scan method were confirmed. Combining a red laser with a CCD camera, the beam pointing accuracy was ~9.3 μrad. We proposed a novel image reconstruction algorithm and demonstrated image reconstruction using the proposed method. The following are the conclusions of our study.

(1) The beams' scan method and reconstruction image algorithm have been checked and were found to be suitable for use in real imaging systems.

(2) The piston aberration was the strongest factor affecting the performance of the imaging system. As argued in this paper, if an appropriate method is chosen for dealing with aberration, good-quality images can be obtained.

(3) The $r0$ of atmospheric turbulence in Changchun was below 3 cm. The diameter of the transmitter beam was ~0.8 cm at the transmitter place, but the size of beams will be expanded to ~8.9 cm in the target plane because their divergence angle is ~0.27 mrad (0.27 mrad × 300 m + 0.8 cm = 8.9 cm). It is easily found that the beams' diameter becomes larger than $r0$ at transmission distances larger than ~100 m. In other words, there is an approximately 200-m-long residual horizontal distance for which the beams' diameter is larger than $r0$. Analysis of the reconstructed images suggests that the FT imaging system can be made insensitive to the uplink atmospheric turbulence by properly designing the transmitter.

(4) The time required for a full scan of a target is ~2.5 h, restricted by the architecture of the mobile platforms. This time can be decreased by improving the transmitter.

All of the hardware components used in this field experiment (except for the green imaging laser) were commercially available components. The imaging capability of the system will be likely improved by using specially designed components. Improving the laser performance is especially important. The work on longer distance uplink transmission is ongoing.

REFERENCES

1. S. Chandler, G. Lukesh, and S. Long, "The impact of dynamic solar panels on long exposure Fourier telescopy," Proc. SPIE **4884**, 130–139 (2003).
2. M. J. Booth, "Adaptive optical microscopy: the ongoing quest for a perfect image," Light Sci. Appl. **3**, e165 (2014).
3. R. B. Holmes, S. Ma, A. Bhowmik, and C. Greninger, "Aperture-synthesis techniques that use very-low-power illumination," Proc. SPIE **2566**, 177–185 (1995).
4. B. F. Campbell, L. Rubin, and R. Holmes, "Experimental demonstration of synthetic aperture imaging through an aberrating medium," Appl. Opt. **34**, 5932–5937 (1995).
5. R. B. Holmes, S. Ma, A. Bhowmik, and C. Greninger, "Analysis and simulation of a synthetic-aperture technique for imaging through a turbulent medium," J. Opt. Soc. Am. A **13**, 351–364 (1996).
6. K. R. MacDonald, J. K. Boger, M. Fetrow, and S. Long, "An experimental demonstration of Fourier telescopy," Proc. SPIE **3815**, 23–29 (1999).
7. J. Mathis, J. Stapp, E. L. Cuellar, J. Cooper, A. Morris, P. Fairchild, D. Hult, K. Koski, L. Ramzel, and M. A. Thornton, "Field experiment performance of the receiver elements for a Fourier telescopy imaging system," Proc. SPIE **5896**, 58960F (2005).
8. D. B. Calia, M. Centrone, F. Pedichini, A. Ricciardi, A. Cerruto, and F. Ambrosino, "Laser guide star pointing camera for ESO LGS facilities," Proc. SPIE **9148**, 91483P (2014).
9. Z. Zhou, B. Xiangli, W. Zhang, Y. Li, and X. Kong, "Fourier telescopy extrapolation based on the sampling theorem," Optik **124**, 5542–5547 (2013).
10. D. Lei, L. Xinyue, L. Xudong, W. Peifeng, and Y. Shuhai, "Improvement of performance and analysis of results of field experiments of Fourier telescope," Acta Opt. Sin. **32**, 0201004 (2012).
11. Z. Yu, L. Xiujuan, X. Aili, C. Bei, and C. Zhiyuan, "Image quality evaluation and analysis in Fourier telescopy for laboratory demonstration," Acta Photon. Sin. **43**, 0311001 (2014).
12. Y. Shu-hai, W. Jian-li, D. Lei, and L. Xin-yue, "Field experiment data processing of Fourier telescopy based on all phase spectrum analysis," Opt. Precis. Eng. **20**, 2275–2282 (2012).
13. L. Sica, "Estimator and signal-to-noise ratio for an integrative synthetic aperture imaging technique," Appl. Opt. **30**, 206–213 (1991).
14. E. L. Cuellar, J. Stapp, and J. Cooper, "Laboratory and field experimental demonstration of a Fourier telescopy imaging system," Proc. SPIE **5896**, 58960D (2005).
15. Z. Yan, Y. Chunping, G. Jing, K. Meiling, and W. Jian, "Spectrum extraction mode for Fourier telescopy in laboratory," High Power Laser Part. Beams **23**, 571–576 (2011).
16. W. T. Rhodes, "Time-average Fourier telescopy: a scheme for high-resolution imaging through horizontal-path turbulence," Appl. Opt. **51**, A11–A16 (2012).
17. J. W. Hardy, Adaptive Optics for Astronomical Telescopes (Oxford University, 1998).
18. W. T. Rhodes, "Closure phase and lucky imaging," Appl. Opt. **48**, A58–A62 (2009).
19. J. E. Ward, W. T. Rhodes, and J. T. Sheridan, "Lucky imaging and aperture synthesis with low-redundancy apertures," Appl. Opt. **48**, A63–A70 (2009).
20. T. J. Brinkley and D. Sandler, "Effect of atmospheric turbulence and jitter on Fourier telescopy imaging systems," Proc. SPIE **3815**, 42–48 (1999).
21. N. D. Ustinov, A. V. Anufriev, A. L. Volpov, Y. A. Zimin, and A. I. Tolmachev, "Active synthesis of the aperture at observation of objects through distorting mediums," Sov. J. Quantum Electron. **14**, 1 (1987).